Study on patterns in square quartz grid dielectric barrier discharge*

LI Cheng[1], GAO Weimin[1], QI Xiaoxiu[1], LI Yuxin[1], PAN Yuyang[2,*], LIU Chang[3,*], DONG Lifang[1,*]

1. College of Physics Science and Technology, Hebei University, Baoding 071002, China
2. Engineering Research Center of Zero-carbon Energy Buildings and Measurement Techniques, Ministry of Education, College of Quality and Technical Supervision, Hebei University, Baoding 071002, China
3. College of Public Health, Hebei University, Baoding 071002, China

Abstract

In this study, a square quartz grid dielectric barrier discharge device is designed, in which a square dot-frame lattice and square cross-dot halo lattice patterns are observed for the first time. These plasma patterns, combined with the quartz grid, constitute a plasma photonic crystal with a square lattice arrangement. Solving the Laplace equation reveals that the applied electric field in the gas gap exhibits a square lattice distribution. The spatiotemporal evolution of these two patterns is characterized using two photomultiplier tubes and an intensified charge-coupled device(ICCD). Results indicate that the square dot-frame lattice pattern consists of two substructures: corner dots and square frame. The corner dots discharge before the square frame. The emission intensities of the corner dots and the square frame differ significantly, with a brightness ratio of approximately 8:5. The square cross-dot halo lattice pattern consists of three substructures: central dots, corner dots, and rhombic frame. The discharge sequence is central dots→corner dots→rhombic frame. The brightness ratio among the three substructures is approximately 17:16:4. This variation indicates that the intensity of electron avalanches differs across distinct substructure locations. Notably, the pattern substructures discharge synchronously across all holes of the quartz grid. The emission spectra of the square cross-dot halo lattice pattern are measured using a spectrograph. The vibrational temperatures at the

* The paper is an English translated version of the original Chinese paper published in Acta Physica Sinica. Please cite the paper as: LI Cheng[1], GAO Weimin[1], QI Xiaoxiu[1], LI Yuxin[1], PAN Yuyang[2,*], LIU Chang[3,*], DONG Lifang[1,*], **Study on patterns in square quartz grid dielectric barrier discharge**. *Acta Phys. Sin.*, 2026, 75(14):140501. doi: 10.7498/aps.75.20260298

central dot, corner dot, and rhombic frame are (2527±55) K, (2559±57) K, and (2611±59) K, respectively, indicating a non-uniform vibrational temperature distribution within each grid hole. Specifically, the relative populations of nitrogen molecules across different vibrational energy levels vary among distinct substructures, revealing that the substructures of the pattern are in different plasma states. Theoretically, the electric field distributions of the square cross-dot halo lattice pattern at different times are simulated by solving the Poisson equation. This effectively elucidates the formation mechanism of the pattern in the square quartz grid dielectric barrier discharge device. This work not only advances the study of pattern dynamics, but also offers a new approach for designing plasma photonic crystals.

Keywords： dielectric barrier discharge; pattern; plasma

DOI： 10.7498/aps.75.20260298

CSTR: 32037.14.aps.75.20260298

1 Introduction

Patterns are fascinating nonlinear self-organization phenomena widely observed in nature and laboratory environments. In nature, patterns exist in various forms, such as animal skin markings, tree rings, and cloud formations[1-3]. Furthermore, patterns are observable in many experimental systems, including Rayleigh-Bénard convection systems, Faraday systems, reaction-diffusion systems, and dielectric barrier discharge (DBD) systems[4-7]. Among these, patterns in DBD systems have attracted significant attention due to their short formation time, stable states, and broad application prospects. DBD is a common method for generating low-temperature plasma. In a typical DBD system, at least one electrode is covered with a dielectric layer, preventing direct conduction current between the two conductive electrodes. Consequently, DBD is usually driven by alternating current or pulsed voltage. Due to its simple structure and low cost, DBD is widely used in ozone generation, material surface modification, pollutant degradation, and plasma medicine[8-12]. In recent years, researchers have discovered that DBD patterns have important applications in the field of plasma photonic crystals[13-17]. In DBD patterns, glow and non-glow regions are distributed in a periodic alternating manner, showing great potential for modulating electromagnetic waves as plasma photonic crystals[18,19]. It is well known that the performance of plasma photonic crystals largely depends on the symmetry and lattice constant of the plasma structure[20-22]. Many studies have found that various plasma photonic crystals with different band structures can be obtained by adjusting the spatial distribution of plasma filaments[18-22]. Therefore, obtaining patterns with different shapes and

symmetries is significant for promoting the application of plasma photonic crystals in fields such as space communication[23,24]. Early pattern research was mainly conducted in parallel-plate DBD devices, where rich pattern types were discovered, such as square patterns, hexagonal patterns, hexagonal superlattice patterns, and spiral patterns[25-29]. Studies have shown that pattern formation depends on the nonlinear resonance of wave vectors[30,31]. Therefore, introducing periodic modulation into a uniform discharge gap will affect the self-organization process of discharge filaments, potentially generating new types of patterns. In recent years, many studies have successfully obtained various patterns by modulating the gas gap. For example, in 2023, Guo et al.[32] obtained a series of patterns with square symmetry by placing specially designed grid photonic crystals in the gas gap. In 2024, Dong et al.[33] obtained various discharge patterns by placing a dielectric with square-arranged circular holes in the gas gap. It is worth noting that in the aforementioned studies, discharge filaments were confined to very small areas. It is well known that when $2r/d$ (r is the radius of the discharge region, and d is the discharge gap spacing) is less than 5, the self-organization behavior of discharge filaments is restricted. Moreover, the boundary shape of the discharge region significantly affects the spatial symmetry and formation process of patterns[34,35]. Therefore, appropriately increasing the discharge area of individual through-holes and changing the shape of the discharge area in the above studies is expected to yield richer self-organized patterns. To this end, this study inserted a quartz grid with square holes into the DBD gas gap to introduce a square lattice electric field. We observed square dot-frame lattice patterns and square cross-dot halo lattice patterns. This further enriches the variety of patterns and provides a reference for research on plasma photonic crystals.

It is well known that the discharge characteristics of DBD patterns are largely influenced by wall charges[36,37]. Wall charges refer to discharge charges accumulated on the dielectric surface. In DBD discharge, as the external electric field strength gradually increases to the gas breakdown threshold, the gas breaks down, generating a large number of charges in the discharge gap. These charges migrate toward the two electrodes and finally deposit on the dielectric surface to form wall charges. During the positive half-cycle of the voltage, as the amount of wall charge accumulated on the dielectric surface increases, the field strength of the built-in electric field generated by the wall charges gradually increases. Since its direction is opposite to that of the external electric field, the wall charges accumulated during the discharge process weaken the total electric field strength in the discharge gap, thereby promoting discharge extinction[38]. When the electrode polarity reverses during the negative half-cycle, the direction of the external electric field changes. The built-in electric field generated by the aforementioned wall charges aligns with the external electric field. At this point, the wall charges promote discharge, allowing the total electric field strength

to reach the breakdown threshold and generate discharge even when the external electric field is very small[39]. Therefore, in parallel-plate DBD devices, since the external electric field in the discharge gap is uniformly distributed, the substructures of patterns usually exhibit an alternating discharge sequence during consecutive positive and negative half-cycles[38-41]. However, in the square quartz grid DBD device, the substructures of the two new types of patterns exhibit the same discharge sequence during positive and negative half-cycles. Analysis reveals that this is related to the non-uniform electric field introduced by the square quartz grid. This study explains the spatiotemporal structure of the patterns by solving the Poisson equation, opening a new direction for research on pattern dynamics in non-uniform electric fields.

This work designed a square quartz grid DBD device. Square dot-frame lattice patterns and square cross-dot halo lattice patterns were observed in this device. By solving the Laplace equation, we obtained the spatial distribution of the external electric field. We used a photomultiplier tube (PMT) and an intensified charge-coupled device (ICCD) camera to investigate the spatiotemporal dynamics of thesquare dot frame lattice pattern and square cross dot halo lattice pattern. We studied the emission spectra of the more complex square cross dot halo lattice pattern using a spectrometer. By solving the Poisson equation, we calculated the electric field at different discharge moments for the square cross-dot halo lattice patterns and discussed the pattern formation mechanism.

2 Experimental Setup

Figure 1 shows a schematic diagram of the experimental setup. The water electrode discharge system consists of two cylindrical containers filled with water. The outer and inner diameters of the containers are 75.0 mm and 65.0 mm, respectively. Both ends of each container are sealed with 1.5 mm thick glass sheets. Copper coils connected to wires are immersed in the water electrodes. The other end of the wires is connected to a sinusoidal AC power supply with a frequency of 50 kHz. The two water electrodes are placed opposite each other along the same axis, creating a 2.5 mm gap between the glass dielectrics of the two water electrodes. A square quartz grid with a thickness of 2.5 mm is placed between the dielectrics to introduce periodic modulation into the discharge gap. The quartz grid is engraved with nine square holes, each with a side length of 6 mm and a spacing of 5 mm. These holes are positioned close to the dielectrics on both sides. Discharge filaments are generated within the holes of the quartz grid. The grid spacing directly affects the distance between plasma discharge filaments in adjacent holes, thereby determining the density of the discharge filaments.

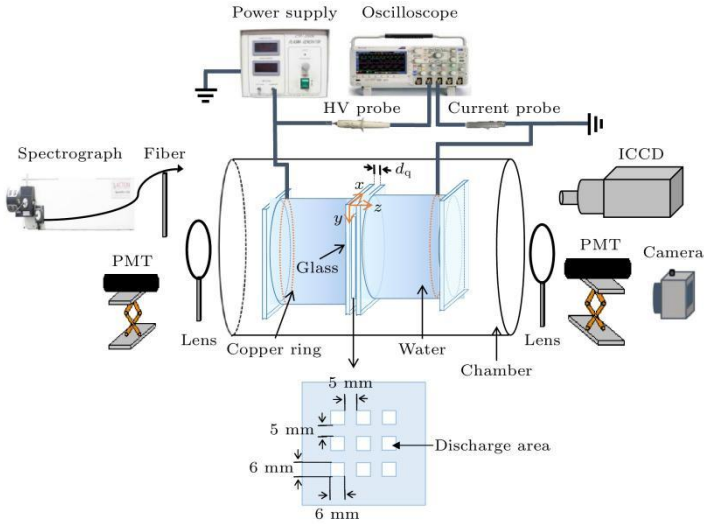


Fig. 1 Schematic of the experimental setup. The square quartz grid has a thickness of d_q = 2.5 mm and is perforated with an array of square holes. Each hole has a side length of 6 mm and a spacing of 5 mm, serving as the discharge gas gap.

The entire discharge apparatus is placed within a reaction chamber with adjustable pressure. The operating pressure in this experiment primarily ranges from 7.5 to 20 kPa. A digital camera (Canon PowerShot G16) records images of pattern evolution during the experiments. Voltage and current are measured using a high-voltage probe (Tektronix P6015A 1000x) and a current probe (Tektronix TCP0030A), respectively. Two photomultiplier tubes (PMT: RCA7265) collect optical signals from the patterns, while an oscilloscope (Tektronix TDS 4054B) measures and records the optical signals along with voltage and current waveforms. An high-speed camera (ICCD, HSFC Pro. 120PH0047) captures instantaneous images of the patterns. The exposure time is set to match the pulse width of the corresponding substructures to distinguish discharges among different substructures. A spectrometer (Acton Advanced SP 2750A, CCD: 1340 × 400 pixels) collects the emission lines of the second positive band system of nitrogen molecules ($C^3\Pi_u \rightarrow B^3\Pi_g$).

Figure 2 presents the electric field distribution in the *x*-*y* cross-section of the air gap at a simulated voltage of 2.88 kV. As shown in Fig. 2, the electric field is strongest at the square apertures and exhibits a square array distribution. Within each aperture, the electric field gradually weakens from the geometric center toward the edges. Consequently, as the voltage increases, discharge initiates first at the center of the square apertures. All plasma in the air gap subsequently arranges into a square array that mirrors the grid shape. Therefore, the square quartz grid plays a crucial role in the initial breakdown of discharge filaments and their subsequent self-organized evolution.

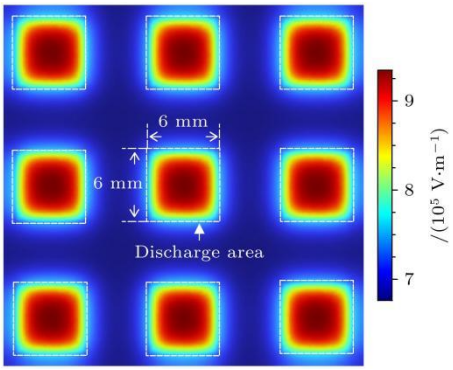


Fig. 2 The electric field distribution in the *x-y* plane with an applied voltage of 2.88 kV. The white dotted box marks the discharge area.

3 Experimental Results and Discussion

3.1 Patterns in the Square Quartz Grid DBD Device

Figure 3 illustrates the evolution of patterns in air at a pressure of p = 14 kPa as the applied voltage increases. When the applied voltage reaches the breakdown threshold of U = 2.88 kV, circular glow discharge filaments appear at the geometric center of each grid via-hole. This forms andot halo lattice pattern, as shown in Fig. 3(a), which aligns with the electric field distribution predictions in Figure 2. As the voltage rises to U = 3.44 kV, the number of discharge filaments within individual grids increases. These filaments exhibit a random and disordered distribution within each via-hole, as depicted in Fig. 3(b). Upon further increasing the voltage to U = 4.26 kV, the positions of the discharge filaments stabilize. The circular discharge filaments become fixed at the four corners of the via-holes, forming a square framework around them. Notably, each via-hole displays an identical filament distribution. Together, these constitutea square dot frame lattice pattern, as shown in Fig. 3(c). Finally, when the voltage reaches U = 4.89 kV, the pattern structure changes. Circular discharge filaments emerge at the geometric centers of the via-holes. The filaments at the four corners move further outward, forming a diamond-shaped framework resembling a glow around these filaments. It is worth noting that each via-hole continues to exhibit the same filament distribution. This results in a square cross dot halo lattice pattern, as illustrated in Fig. 3(d).

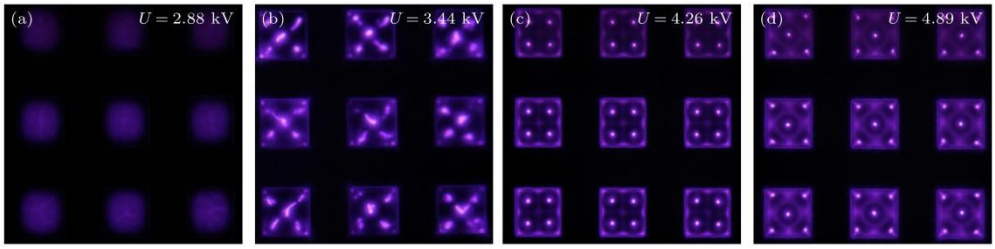


Fig. 3 Bifurcation of the discharge pattern with increasing applied voltage: (a) Dot halo lattice pattern, *U* = 2.88 kV; (b) Random discharges, *U* = 3.44 kV; (c) Square dot frame lattice pattern, *U* = 4.26 kV; (d) Square cross dot halo lattice pattern, *U* = 4.89 kV. The experiment was conducted in air at a gas pressure of *p* = 14 kPa.

To investigate the effects of pressure and voltage on pattern evolution, Fig. 4 presents the phase diagram of pattern evolution as a function of applied pressure *p* and voltage *U*. Figures 4(a)—(d) correspond to the patterns shown in Figs. 3(a)—(d), with their existence ranges indicated by blue, yellow, orange, and pink regions, respectively. Clearly, these patterns can stably exist within specific voltage and pressure ranges. When pressure is held constant, these patterns emerge sequentially as voltage increases. As pressure increases, the required applied voltage for these patterns gradually rises. In summary, pattern evolution is observable within the range of 7.5—20 kPa, and the discharge voltage gradually increases with increasing pressure.

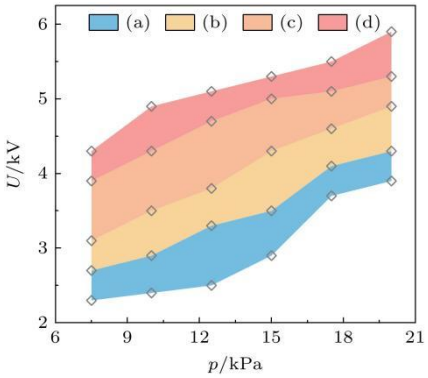


Fig. 4 Phase diagram of discharge patterns as functions of the gas pressure *p* and the voltage *U*

In summary, square dot frame lattice pattern and square cross dot halo lattice pattern were obtained for the first time in a square quartz mesh DBD device. To investigate the discharge characteristics of these patterns, spatiotemporal dynamics measurements were performed on both patterns using a PMT and an ICCD, respectively.

3.2 Spatiotemporal Dynamics Measurement of Square Dot Frame Lattice Pattern

Given the identical distribution of discharge filaments within each through-hole, this study first investigates the structure and characteristics of a single through-hole to simplify the analysis. Figure 5(a) presents the spatial light intensity distribution within a single through-hole. The height of the three-dimensional light intensity distribution is positively correlated with the light intensity, and the two-dimensional image at the base represents the projection of the three-dimensional distribution. It is evident that there is

a significant difference in brightness between the corner dots (C_1) and the square frames (F_1). Measurements indicate that the light intensity values for C_1 and F_1 are 255 and 153, respectively, yielding a brightness ratio of approximately 8:5.

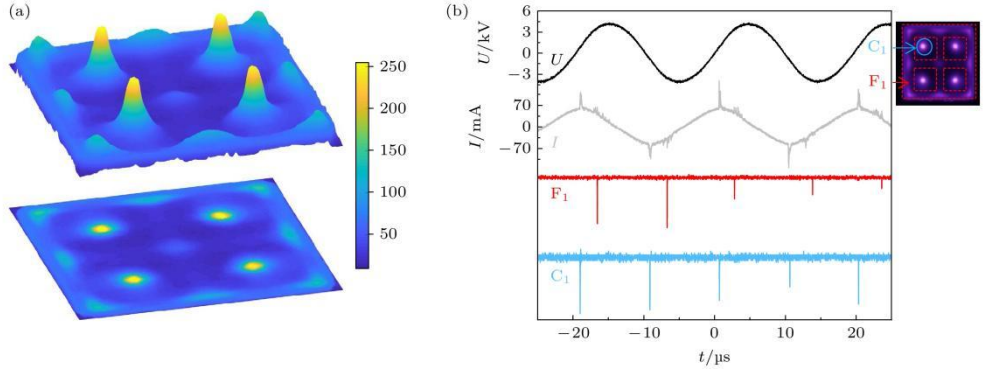


Fig. 5 Light intensity distribution (a) and spatiotemporal dynamics measurement (b) of the square dot frame lattice pattern.

To clarify the discharge sequence of the substructures, a photomultiplier tube (PMT) was employed to investigate the temporal correlation of different substructures within a single through-hole. Figure 5(b) presents the optical signals for C_1 and F_1. The results indicate that both C_1 and F_1 discharge during the voltage rising edge in each half-cycle. Specifically, C_1 discharges prior to F_1, with C_1 corresponding to the first pulse and F_1 corresponding to the subsequent current pulse. Consequently, the discharge sequence for the square dot frame lattice pattern is $C_1 \rightarrow F_1$.

To investigate the discharge behavior of the substructures within the square dot frame lattice pattern across all through-holes, an intensified charge-coupled device (ICCD) camera was used to capture instantaneous images of the pattern. Figure 6(a) displays the voltage and current waveforms of the pattern. Based on the spatiotemporal dynamics measurements shown in Fig. 5(b), C_1 discharges during the first pulse, while F_1 discharges during the subsequent current pulse. To capture the discharge of different substructures, two channels of the ICCD were utilized to select specific time intervals for imaging: Δt_1 = 300 ns, which encompasses the first current pulse, and Δt_2 = 1520 ns, which encompasses the subsequent current pulse. It is important to note that the sequential nature of the substructure discharges means that the selection of exposure intervals significantly influences the imaging results. Figures 6(b) and 6(c) present the instantaneous images accumulated 30 times under the exposure times Δt_1 and Δt_2, respectively. Figure 6(d) shows the superposition of Figs. 6(b) and 6(c). As observed in Fig. 6(d), C_1 discharges during the first current pulse, and F_1 discharges during the subsequent current pulse. Furthermore, the corresponding substructures discharge in each through-hole, forming an overall square array arrangement. Based on the comprehensive measurement and analysis above, the square dot frame lattice pattern consists of two nested substructures: the corner dots (C_1) and the square frames (F_1). Additionally, the substructures within each through-hole exhibit high simultaneity in

their discharge.

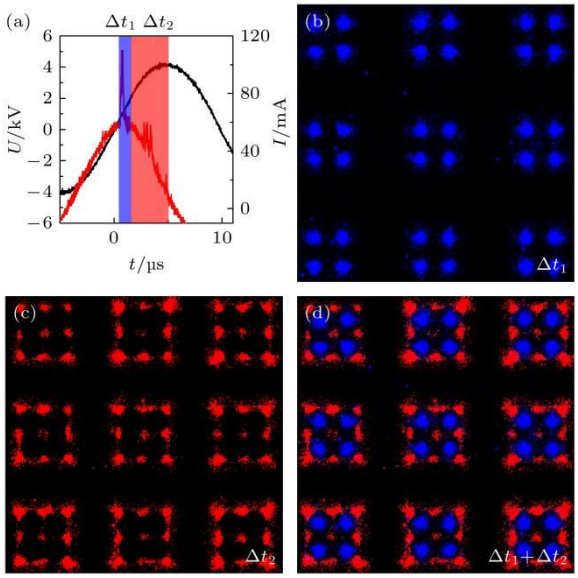


Fig. 6 Instantaneous images of the square dot frame lattice pattern: (a) Voltage and current waveforms of the pattern (Δt_1 = 300 ns, Δt_2 = 1520 ns); (b), (c) images corresponding to Δt_1 and Δt_2 in (a), respectively, integrated over 30 voltage cycles; (d) superposition of (b) and (c).

3.3 Spatiotemporal Dynamics Measurement of Square Cross Dot Halo Lattice Pattern

To analyze the discharge structure within the square cross dot halo lattice pattern, Fig. 7(a) presents the light intensity distribution in a single through-hole. Significant differences in luminous intensity are observed among the bright spot at the geometric center (S_2), the four corner points (C_2), and the rhombic frame (F_2). The light intensity values for S_2, C_2, and F_2 are 255, 242, and 60, respectively, yielding a brightness ratio of approximately 17∶16∶4. Notably, the intensity difference between C_2 and F_2 exceeds that between C_1 and F_1. Since plasma light intensity correlates positively with the severity of electron avalanches, this indicates a greater disparity in electron avalanche intensity between the C_2 and F_2 positions than between C_1 and F_1. Consequently, the square cross dot halo lattice pattern likely consists of three nested substructures: S_2, C_2, and F_2.

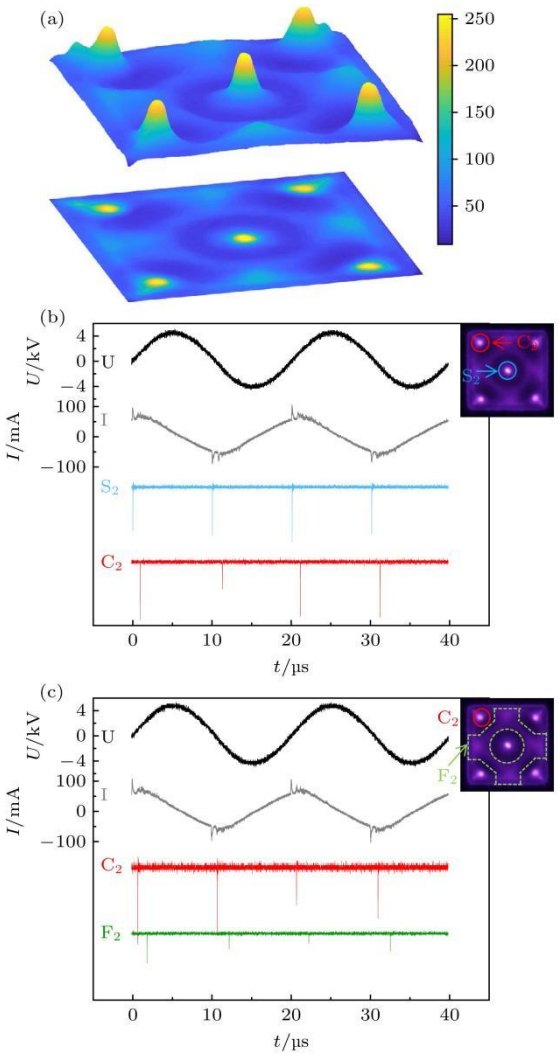


Fig. 7 Light intensity distribution and spatiotemporal dynamics measurement of the square-cross dot halo lattice pattern: (a) Light intensity distribution of the pattern; (b) Optical signals of C_2 and S_2; (c) Optical signals of C_2 and F_2.

To clarify the discharge sequence of the pattern substructures, a photomultiplier tube (PMT) was employed to measure the temporal correlation of different substructures within a single via. Figure 7(b) presents the optical signals for S_2 and C_2. The optical signal of S_2 corresponds to the first pulse, while that of C_2 corresponds to the second pulse, indicating that S_2 discharges before C_2. Figure 7(c) displays the optical signals for C_2 and F_2, revealing that F_2 discharges after C_2. Consequently, the discharge sequence of the substructures is $S_2 \rightarrow C_2 \rightarrow F_2$.

To further investigate the discharge behavior of substructures in the square cross dot halo lattice pattern holesin all holes, an intensified charge-coupled device (ICCD) camera was used to capture instantaneous images of the pattern for individual pulses. Figure 8(a) shows the voltage and current waveforms of this pattern, where the widths of the three current pulses are Δt_1 = 300 ns, Δt_2 = 820 ns, and Δt_3 = 1100 ns, respectively. Figures 8(b)-(d) correspond to instantaneous images accumulated 30

times under exposure times of Δt_1, Δt_2, and Δt_3, respectively. Figure 8(e) is the superimposed image of Figs. 8(b)-(d). As shown in Fig. 8(e), S_2 discharges during the first current pulse, C_2 during the second, and F_2 during the final continuous pulse. The substructures in each via exhibit high discharge simultaneity, forming an overall square array arrangement. In summary, the square cross dot halo lattice pattern consists of three nested substructures: S_2, C_2, and F_2. The discharge sequence is $S_2 \rightarrow C_2 \rightarrow F_2$, and the substructures in all holes demonstrate high discharge simultaneity, resulting in a global square array distribution.

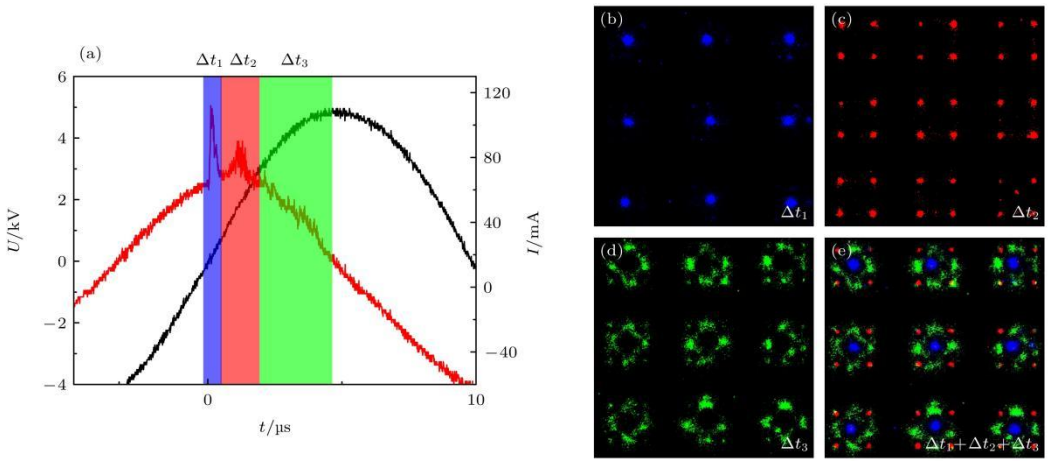


Fig. 8 Instantaneous images of the square cross-dot halo lattice pattern: (a) Voltage and current waveforms of the pattern (Δt_1 = 300 ns, Δt_2 = 820 ns, Δt_3 = 1100 ns); (b)-(d) Images corresponding to Δt_1, Δt_2, and Δt_3 in panel (a), respectively, integrated over 30 voltage cycles; (e) Superposition of panels (b)-(d).

It is worth noting that the discharge sequence of the aforementioned two pattern substructures does not fully align with the magnitude of the applied electric field. According to the applied electric field distribution shown in Fig. 2, the electric field within the through-hole gradually weakens from the geometric center toward the edge. However, in the square dot frame lattice pattern, the corner points C_1 discharge first, while the central point F_1 discharges later. In the square cross-dot halo lattice pattern, the central point S_2 discharges before the corner points C_2, and the corner points C_2, which are farther from the center, discharge before the diamond-shaped frame F_2. This indicates that the discharge behavior of the patterns is not only related to the applied electric field but also influenced by other factors. To investigate the discharge mechanism of patterns in the square quartz grid device, we next study the more complex square cross-dot halo lattice pattern.

3.4 Spectral Diagnosis of Plasma Parameters

Figure 9(a) presents the emission lines of the nitrogen molecule second positive band system ($C^3\Pi_u \rightarrow B^3\Pi_g$) for different substructures in the square cross-dot halo lattice pattern. It is well known that the intensity of diatomic molecular band systems ($I_{v'v''}$) is

determined by the following equation:

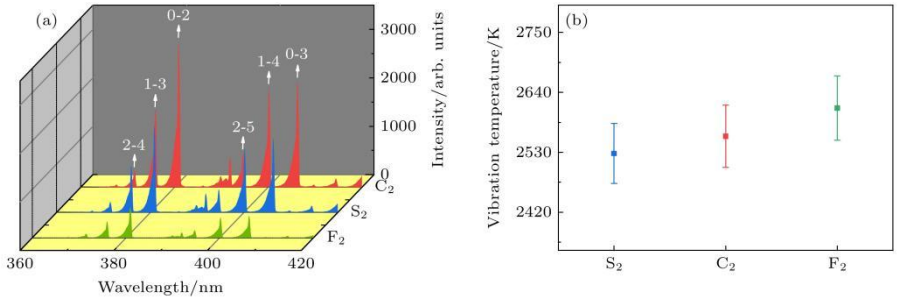


Fig. 9 Emission spectra of the pattern: (a) N_2 emission spectra of substructures within the 360-420 nm range for the square cross-dot halo lattice pattern; (b) scatterplot of vibrational temperatures for the square cross-dot halo lattice pattern.

$$I_{v'v''} = hcvN_{v'}A_{v'v''}, \quad (1)$$

Here, v denotes the wavenumber of the emitted photon; v' and v'' represent the upper and lower vibrational quantum numbers, respectively; h is the Planck constant; c is the speed of light; $N_{v'}$ is the number of molecules in the upper energy quantum state; and $A_{v'v''}$ is the transition probability between the corresponding two quantum states. This study assumes that the plasma can achieve approximate local thermal equilibrium. Consequently, the population distribution of particles in the upper energy state satisfies the Boltzmann distribution:

$$N_{v'} = N_0 \mathrm{e}^{-E_{v'}/k_B T_v}, \quad (2)$$

Here, N_0 is the normalization constant; $E_{v'}$ denotes the vibrational energy of the v' energy level; and k_B is the Boltzmann constant. By combining Equation (1) and Equation (2), we obtain

$$\ln \frac{I_{v'v''}}{vA_{v'v''}} = C - \frac{E_{v'}}{k_B T_v}, \quad (3)$$

Here, C is a constant. It is evident that $\ln \frac{I_{v'v''}}{vA_{v'v''}}$ varies linearly with $E_{v'}$. Consequently, we plot $\ln \frac{I_{v'v''}}{vA_{v'v''}}$ on the vertical axis against $E_{v'}$ on the horizontal axis. The vibrational temperature T_v is then determined from the slope of the line fitted to the experimental data. To minimize calculation errors, this study estimates the vibrational temperature using two sets of vibrational bands: Δv = -2 (0-2, 1-3, 2-4) and Δv = -3 (0-3, 1-4, 2-5), for estimating vibrational temperature[29,42,43]. The results are presented in Fig. 9(b). The vibrational temperature at the central point S_2 is (2527±55) K, at the corner point C_2 is (2559±57) K, and at the diamond-shaped frame F_2 is (2611±59) K. As shown in Fig. 9(b), although the measurement values overlap within the error range, the mean vibrational temperature exhibits a gradual increasing trend from S_2 to C_2 and then to F_2. This indicates a certain degree of non-uniformity in the distribution of vibrational temperature within each through-hole. Specifically, the relative population of nitrogen

molecules across different vibrational energy levels varies among the different substructures.

Comparing the distribution of vibrational temperature with the applied electric field distribution in Fig. 2 reveals that they do not correspond perfectly. Specifically, the applied electric field intensity at position S_2 is stronger than that at C_2 and F_2, yet its mean vibrational temperature is slightly lower than those at C_2 and F_2, showing an opposite distribution characteristic. In contrast, between F_2 and C_2, the applied electric field at F_2 is greater than that at C_2, and its mean vibrational temperature is also higher than that at C_2, indicating a consistent trend between the applied electric field and vibrational temperature. Analysis suggests that the discharge behavior of the pattern is influenced not only by the applied electric field but also by the accumulation of wall charges. To further elucidate the discharge mechanism of the pattern, the following section will discuss and analyze the formation mechanism by solving the Poisson equation.

3.5 Spatiotemporal Evolution of the Electric Field

In the study of DBD patterns, wall charges are generally regarded as the key factor determining pattern distribution[17,44,45]. During the discharge process, space charges deposit on the dielectric surface through filamentary discharge channels to form wall charges. Although the "internal electric field" generated by space charges affects the formation and development of discharge channels at the moment of discharge[46], the spatial position and discharge sequence of pattern substructures mainly depend on the electric field distribution before breakdown. This distribution is predominantly modulated by wall charges, which exhibit a "memory effect"[44,45,47,48]. Therefore, analyzing the wall charge electric field using electrostatic field simulation is sufficient to explain the formation and development of patterns, with negligible error in mechanism analysis.

To investigate the formation mechanism of patterns in the square quartz grid device, we used COMSOL Multiphysics software to solve the Poisson equation. We simulated and calculated the electric field on the *x*-*y* cross-section of the air gap at different discharge moments. Considering the similarity of discharge in each through-hole, we analyzed the electric field distribution within a single through-hole.

Poisson equation:

$$\nabla^2\psi = -\frac{\rho}{\varepsilon_r\varepsilon_0}, \tag{4}$$

Here, $\boldsymbol{\psi}$ denotes the electric potential; ρ represents the charge density; ε_r indicates the relative permittivity; and ε_0 signifies the vacuum permittivity. The relationship between the electric field $\boldsymbol{E}$ and the electric potential $\boldsymbol{\psi}$ in the air gap is given by

$$\boldsymbol{E} = -\nabla\psi. \tag{5}$$

To calculate the charge density ρ on the dielectric surface, integrate the corresponding current pulses for S_2, C_2, and F_2 in Fig. 8(a):

$$Q = \int_{t_1}^{t_2} I\mathrm{d}t. \quad (6)$$

The transferred charge quantities for the corresponding discharge periods are determined to be Q_{S_2} = 11.7×10^{-9} C, Q_{C_2} = 15.62×10^{-9} C, and Q_{F_2} = 13.78×10^{-9} C. Subsequently, the following formula is applied:

$$\rho = \frac{Q}{nS}, \quad (7)$$

Here, *n* denotes the number of discharge filaments, *S* represents the area of the discharge filaments, and *Q* indicates the transferred charge of the discharge filaments. For C_2 and S_2, *n* refers to the total number of discharge channels in the air gap, while *S* corresponds to the projected area of the discharge filaments on the glass dielectric. For F_2, *n* represents the number of frames in all through-holes, and *S* denotes the area of the frame projected onto the glass dielectric. Due to the irregular shapes of the discharge filaments, area calculations require approximations. For instance, C_2 and S_2 are approximated as circles, whereas F_2 is approximated as a combination of rectangles and connecting lines. Consequently, this process introduces minor experimental errors. The calculated charge densities accumulated on the dielectric surface for S_2, C_2, and F_2 are ρ_{S_2} = 7.26×10^{-4} C/m^2, ρ_{C_2} = 6.89×10^{-4} C/m^2, and ρ_{F_2} = 1.52×10^{-4} C/m^2, respectively. The results indicate that the surface charge density decreases in the order S_2 -C_2 -F_2. This trend aligns closely with the intensity order of the different substructures shown in Fig. 7(a).

To investigate the role of wall charges in the pattern discharge process, we simulated the electric field distribution within a single through-hole at different discharge moments, as illustrated in Fig. 10. Figure 10(a) presents the voltage and current waveforms for the square cross dot halo lattice pattern during the positive half-cycle of the voltage. To visually clarify the shape and position of each substructure within the pattern, Fig. 10(b) provides a schematic diagram of the pattern structure. In this diagram, the small red circles at the four corners represent C_2, the large blue circle at the center represents S_2, and the frame composed of green rectangles and connecting lines represents F_2. Figures 10(c) through 10(e) display the electric fields within a single through-hole at times t_1, t_2, and t_3, respectively. The corresponding pattern substructures discharging at these moments are shown in Figs. 10(c1) through 10(e1). Figure 10(c) depicts the electric field distribution in the air gap during the initial rising edge of the voltage (U_1 = 0 kV, t = t_1). At this stage, the maximum electric field intensity is located at the center of the through-hole. Consequently, the central point S_2 discharges during the Δt_1 interval, as shown in Fig. 10(c1). After the central point discharges, the accumulated wall charges generate an electric field opposite to the

external field. The resulting electric field distribution after the S_2 discharge is shown in Fig. 10(d) (U_2 = 0.88 kV, $t = t_2$). As indicated in Fig. 10(d), the field strength is highest in the four corner regions at this time. Therefore, the corner points C_2 discharge during the Δt_2 interval, as illustrated in Fig. 10(d1). The wall charges generated by the corner point discharges also produce an opposing electric field. The resulting electric field distribution is shown in Fig. 10(e) (U_3 = 2.88 kV, $t = t_3$). The wall charges accumulated from the S_2 and C_2 discharges create an opposing electric field, leading to higher field strengths in areas distant from S_2 and C_2. Consequently, the next discharge structure is the rhombic frame, as shown in Fig. 10(e1). When the polarity of the applied voltage reverses, the discharge of the pattern substructures during the negative half-cycle resembles that of the positive half-cycle. The corresponding electric field distributions and discharge structures are shown in Figs. 10(f) through 10(h) and Figs. 10(f1) through 10(h1), respectively. Clearly, the pattern substructures repeat the discharge process observed during the positive half-cycle.

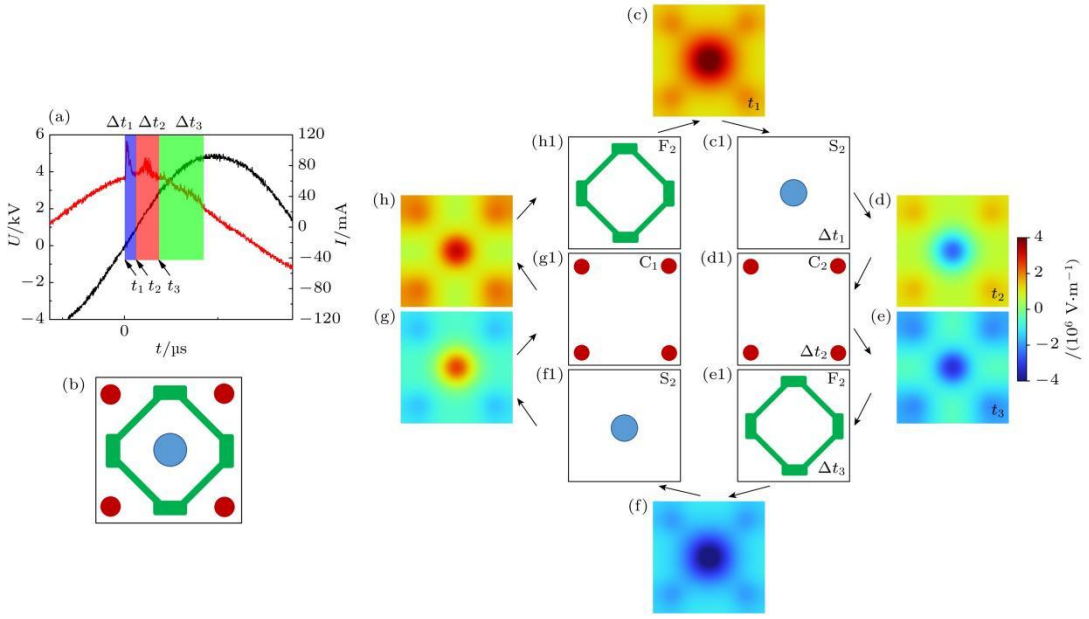


Fig. 10 Electric fields and substructures schematic diagrams of the square cross dot halo lattice pattern at different discharge moments: (a) Voltage and current waveforms; (b) schematic diagram of the pattern structure; (c)–(h) electric field distributions at different moments; (c1)–(h1) schematic diagrams of the substructures under the electric fields in Figure (c)–(h), respectively.

Figure 10 illustrates the spatiotemporal evolution of the electric field and discharge. The formation of patterns results from the combined action of the applied electric field and wall charges. The applied electric field and the wall charge electric field jointly determine the discharge sequence of substructures. After a substructure discharges, the direction of the wall charge electric field at that location reverses. This reversal influences the subsequent discharge. Through this cyclic interaction, patterns with stable spatiotemporal structures ultimately form.

In the square quartz grid dielectric barrier discharge device, the square array electric field couples with the self-organization process of discharge filaments. This coupling generates patterns with square symmetry, thereby promoting the development of pattern dynamics. These plasma patterns align periodically with the quartz grid, providing a physical basis for the design of plasma photonic crystals. Plasma is a dispersive medium. Its equivalent dielectric constant depends on the frequency of incident electromagnetic waves. This characteristic endows plasma photonic crystals with novel properties distinct from those of conventional photonic crystals[49-52]. For conventional photonic crystals composed of solid materials, the tunable frequency range of electromagnetic waves is typically fixed after fabrication. This limitation arises because key parameters determining the position and width of the photonic bandgap, such as the dielectric constant and lattice constant, are difficult to adjust post-fabrication. In contrast, plasma photonic crystals allow dynamic tuning of their dielectric and lattice constants by adjusting external parameters such as voltage and gas pressure[53,54]. This capability offers potential for fabricating tunable microwave devices. In this setup, adjusting discharge parameters effectively controls the patterns within the through-holes. This process creates various periodic structures with square symmetry, providing insights and references for research on plasma photonic crystals.

4 Conclusion

This study designed a square quartz grid dielectric barrier discharge device to achieve spatial modulation of discharge filaments. We observed square dot frame lattice pattern and square cross dot halo lattice pattern for the first time. By combining experimental measurements with theoretical analysis, we systematically revealed the spatiotemporal dynamic behaviors and formation mechanisms of these two novel patterns. Simulations of the spatial distribution of the applied electric field using the Laplace equation indicated that the introduction of the quartz grid caused the applied electric field in the air gap to exhibit a square array distribution. Spatiotemporal resolved measurements using a photomultiplier tube (PMT) and an intensified charge-coupled device (ICCD) revealed that the square dot frame lattice pattern forms through the sequential discharge of two substructures: corner points and a square frame. The square cross dot halo lattice pattern forms through the sequential discharge of three substructures: a central point, corner points, and a rhombic frame. Notably, the discharge of substructures at each through-hole exhibits high simultaneity. Spectroscopic measurements of nitrogen molecular emission lines in the square cross dot halo lattice pattern allowed calculation of the vibrational temperatures of the substructures. The results indicated that these substructures exist in different plasma states. To investigate the discharge mechanism of patterns in the square quartz grid device, we solved the Poisson equation using COMSOL Multiphysics. We simulated the electric field distribution of the square cross

dot halo lattice pattern at different discharge moments. The findings confirmed that pattern formation results from the combined action of the applied electric field and the wall charge electric field.

This work introduced a quartz grid into the DBD air gap to obtain novel patterns with regular symmetry. This approach enriches the research system of pattern dynamics. Furthermore, these plasma patterns and the quartz grid jointly constitute a square periodic structure, providing a physical basis for the design of plasma photonic crystals.

References

[1] Joron M, Jiggins C D, Papanicolaou A, McMillan W O 2006 *Heredity* **97** 157

[2] Rietkerk M, Bastiaansen R, Banerjee S, Koppel J, Baudena M, Doelman A 2021 *Science* **374** 169

[3] Kogelschatz U 2010 *J. Phys. Conf. Ser.* **257** 012015

[4] Rogers J L, Schatz M F, Brausch O, Pesch W 2000 *Phys. Rev. Lett.* **85** 4281

[5] Epstein T, Fineberg J 2006 *Phys. Rev. E* **73** 055302

[6] Kameke A V, Huhn F, Muñuzuri A P, Muñuzuri V P 2013 *Phys. Rev. Lett.* **110** 088302

[7] Breazeal W, Flynn K M, Gwinn E G 1995 *Phys. Rev. E* **52** 1503

[8] Wymenga L F A, van Turnhout J, Ghaffarian Niasar M, van Zeijl H W, van Driel W D, Zhang G Q 2026 *J. Phys. D: Appl. Phys.* **59** 025203

[9] Zhu X, Guan X H, Luo Z R, Wang L Y, Dai L Y, Wu Z X, Fan J J, Cui X L, Akram S, Fang Z 2024 *J. Phys. D: Appl. Phys.* **57** 275203

[10] Tański M, Podliński J, Berendt A, Mizeraczyk J 2024 *Appl. Sci.* **14** 11596

[11] Park J, Cha M S 2025 *J. Phys. D: Appl. Phys.* **58** 105207

[12] Hong C, Kim Y 2020 *IEEE Trans. Plasma Sci.* **48** 3890

[13] Peng B F, Wang R Z, Li J, Jiang N, Yuan D K, Chen Z Q, Lei Z P, Kang A L, Song J C 2024 *Appl. Phys. Lett.* **125** 144102

[14] Li Y H, Yan Z H, Yan Z H, Li C, Pan Y Y, Dong L F 2025 *Acta. Phys. Sin.* **74** 225201

[15] Wang J, Li J, Lei B Y, Ran S, Xu B, Liu Y H, Li X Z, Wang Y S, Tang J, Zhao W, Duan Y X 2021 *Plasma Sources Sci. Technol.* **30** 045002

[16] Li C, Yan Z H, Qi X X, Li Y X, Pan Y Y, Dong L F 2025 *Acta. Phys. Sin.* **74** 225202

[17] Kogelschatz U 2002 *IEEE Trans. Plasma Sci.* **30** 1400

[18] Fan W L, Liu C Y, Gao K Y, Liang Y Q, Liu F C 2021 *Phys. Lett. A* **396** 127223
[19] Li R, Wang Q H, Liu F C, Gao K Y, Hou X H, Jia M M, Li Q, Fan W L 2024 *Plasma Sci. Technol.* **26** 064008
[20] Liu F C, Liu Y N, Liu Q, Wu Z C, Liu Y H, Gao K Y, He Y F, Fan W L, Dong L F 2022 *Plasma Sources Sci. Technol.* **31** 025015
[21] Wang S, Liu S, Hou X H, Liu F C, Wu Z C, He Y F, Fan W L 2024 *Phys. Lett. A* **525** 129850
[22] Zhang L, Ouyang J T 2014 *Phys. Plasmas* **21** 103514
[23] Poddar H, Nayak C, Behera J K, Dash D 2024 *Opt. Mater.* **152** 115545
[24] Zhang H F 2018 *AIP Adv.* **8** 015304
[25] Dong L F, Fan W L, He Y F, Liu F C, Li S F, Gao R L, Wang L 2006 *Phys. Rev. E* **73** 066206
[26] Feng J Y, Dong L F, Li C X, Liu Y, Du T, Hao F. 2017 *Plasma Sci. Technol.* **19** 055401
[27] Dong L F, Shang J, He Y F, Bai Z G, Liu L, Fan W L 2012 *Phys. Rev. E* **85** 066403
[28] Dong L F, Liu W B, Wang Y J, Zhang X P 2014 *IEEE Trans. Plasma Sci.* **42** 2
[29] Li C X, Feng J Y, Wang S C, Li C, Ran J X, Pan Y Y, Dong L F 2024 *Plasma Sci. Technol.* **26** 085401
[30] Hoyuelos M, Walgraef D, Colet P, Miguel M S 2002 *Phys. Rev. E* **65** 046620
[31] Bai Z G, Liu F C, Dong L F 2015 *Acta. Phys. Sin.* **64** 210505
[32] Guo L T, Pan Y Y, Yu G L, Wang C Y, Gao K Y, Fan W L, Dong L F 2023 *Plasma Sci. Technol.* **25** 085501
[33] Dong L F, Zhang L J, He Y N, Wei T, Li Y H, Li C, Pan Y Y 2024 *Appl. Phys. Lett.* **125** 104101
[34] Duan X X, Ouyang J T, Zhao X F, He F 2009 *Phys. Rev. E* **80** 016202
[35] Feng J Y, Dong L F, Wei L Y, Fan W L, Li C X, Pan Y Y 2016 *Phys. Plasmas* **23** 093502
[36] Guo B G, Wei W, Shinoda T, Liu C L 2007 *Appl. Phys. Lett.* **90** 101501
[37] Ouyang J T, He F, Feng S, Yu Z N, Liang Z H, Wang J Q 2006 *Appl. Phys. Lett.* **89** 031504
[38] Dong L F, Li B, Lu N, Li X C, Shen Z K 2012 *Phys. Plasmas* **19** 052304
[39] Cui Y Q, Dong L F, Gao X, Wei L Y, Liu W B, Feng J Y, Pan Y Y 2017 *Phys. Plasmas* **24** 084502
[40] Dong L F, Liu W L, Wang H F, He Y F, Fan W L, Gao R L 2007 *Phys. Rev. E* **76** 046210
[41] Dong L F, Yin Z Q, Wang L, Fu G S, He Y F, Chai Z F, Li X C 2003 *Thin Solid*

Films **435** 120

[42] Li Y H, Pan Y Y, Tian M, Wang Y, He Y N, Zhang J H, Chu J H, Dong L F 2023 *Phys. Plasmas* **30** 033502

[43] Feng J Y, Pan Y Y, Li C X, Liu B B, Dong L F 2020 *Phys. Plasmas* **27** 063516

[44] Stollenwerk L, Laven J G, Purwins H G 2007 *Phys. Rev. Lett.* **98** 255001

[45] Stollenwerk L, Amiranashvili S, Boeuf J P, Purwins H G 2006 *Phys. Rev. Lett.* **96** 255001

[46] Zhang J, Tang W W, Wang Y H, Wang D Z 2023 *Plasma Sources Sci. Technol.* **32** 055005

[47] Choi K C, Rhee B J, Lee H N 2003 *IEEE Trans. Plasma Sci.* **31** 3

[48] Yin Z Q, Wang L, Dong L F, Li X C, Chai Z F 2003 *Acta Phys. Sin.* **52** 929

[49] Zhou M J, Tan H Y, Zhuge L J, Wu X M 2024 *Plasma Sci. Technol.* **26** 115501

[50] Sakai O, Sakaguchi T, Tachibana K 2007 *Contrib. Plasma Phys.* **47** 96

[51] Qi L M, Yang Z Q, Lan F, Gao X, Li D Z 2010 *Chin. Phys. B* **19** 034210

[52] Wang J, Liu S, Fan W L, Wang S, Lu C C, He Y F, Liu F C, Hu X Y 2024 *Front. Optoelectron.* **17** 34

[53] Dong L F, Li Y H, Qi X X, Fan W L, Li R, Liu S, Pan Y Y 2025 *Opt. Express* **33** 37246

[54] Ma J, Wang Z G, Liu X J, Zhang S Q, Liang Y, Wu X Y 2017 *Physica E* **89** 61